PCCP

Accepted Manuscript

ROYAL SOCIETY OF CHEMISTRY

www.rsc.org/pccp

Physical Chemistry Chemical Physics RSCPublishing

ARTICLE

Lithium-Doping Inverts the Nanoscale Electric Field at the Grain Boundaries in $Cu_2ZnSn(S,Se)_4$ and Increases Photovoltaic Efficiency

Cite this: DOI: 10.1039/xoxxoooooox

Received ooth January 2012,
Accepted ooth January 2012

DOI: 10.1039/xoxxoooooox

www.rsc.org/

H. Xin[a,d], S. M. Vorpahl[b,d], A. D. Collord[a,d], I. L. Braly[a,d], A. R. Uhl[a,d], B. W. Krueger[c], D. S. Ginger[b,d], and H. W. Hillhouse[a,d]*

Passive grain boundaries (GBs) are essential for polycrystalline solar cells to reach high efficiency. However, the GBs in $Cu_2ZnSn(S,Se)_4$ have less favorable defect chemistry compared to $CuInGaSe_2$. Here, using scanning probe microscopy we show that lithium doping of $Cu_2ZnSn(S,Se)_4$ changes the polarity of the electric field at the GB such that minority carrier electrons are repelled from the GB. Solar cells with lithium-doping show improved performance and yield a new efficiency record of 11.8% for hydrazine-free solution-processed $Cu_2ZnSn(S,Se)_4$. We propose that lithium competes for copper vacancies (forming benign isoelectronic Li_{Cu} defects) decreasing the concentration of Zn_{Cu} donors and competes for zinc vacancies (forming a Li_{Zn} acceptor that is likely shallower than Cu_{Zn}). Both phenomena may explain the order of magnitude increase in conductivity. Further, the effects of lithium doping reported here establish that extrinsic species are able to alter the nanoscale electric fields near the GBs in $Cu_2ZnSn(S,Se)_4$. This will be essential for this low-cost Earth abundant element semiconductor to achieve efficiencies that compete with $CuInGaSe_2$ and CdTe.

Introduction

Thin film photovoltaics using copper zinc tin sulfoselenides, $Cu_2ZnSn(S,Se)_4$ or CZTSSe, are one of the most promising materials for terawatt scale PV production. The high crustal abundance of the constituent elements and high mineral extraction and production rates mean that CZTSSe may provide ultra-low cost electrical power without the financial risks associated with tellurium in CdTe or indium in $CuInGaSe_2$ (CIGSe). However, the record CZTSSe solar cell has an efficiency of 12.6%,[1] while several CIGSe devices with efficiencies greater than 20% have been reported.[2, 3] This deficit is known to be due to several (potentially overlapping) physical phenomena in CZTSSe including the presence of local electrostatic potential fluctuations,[4] cation disorder, large populations of defects and defect clusters,[5] and less passive grain boundaries.[6, 7] Some or all of these cause decreased open circuit voltage and lower fill factor.[8] As a result, a better fundamental understanding of the materials chemistry of CZTSSe is needed along with the development of experimental techniques to remedy the problems.

Many of the current paradigms for understanding the defect chemistry of CZTSSe are based on the knowledge of the defect chemistry of CIGSe since they are so closely related structurally. It is well known that the addition of sodium into CIGSe absorber layers during film processing is critical to produce high efficiency CIGSe solar cells. The effect was discovered unintentionally when soda-lime glass was used as the substrate over 20 years ago.[9, 10] The current understanding of the role of sodium is based on several decades of experimental evidence[9-17] and *ab initio* calculations[18-20] that indicate that sodium increases the acceptor concentration, passivates defects, and aides grain growth leading to larger open-circuit voltage and fill factor. While the exact mechanism is still debated, it has been argued that sodium: (1) increases the p-type carrier concentration by providing a shallow acceptor Na_{In},[13, 18] (2) reduces the concentration of the deep level created by In_{Cu} defects by occupying copper vacancies,[13, 17, 18, 20] (3) passivates grain boundaries by promoting oxidation of V_{Se} defects,[11, 16] (4) assists grain growth by forming Na_2Se_x that acts as a selenium fluxing agent,[21] or (5) modifies the electrostatics at the GB[19, 22] to repel holes from the GB and perhaps improve minority carrier collection. While several of

these effects may occur in parallel, there is particularly strong experimental evidence for sodium effecting band bending. Jiang et al.[19] showed that sodium creates a downward bend in the CB at the GBs of high quality CIGSe that leads to devices with 19.2% efficiency. The downward bend is indicated by a positive spike in the contact potential difference (CPD) measured by scanning Kelvin probe microscopy (SKPM). However, Hanna et al.[23] have argued that not all GBs are the same with regard to their electrostatics. Films with (112) or random orientation were shown to have a positive spike in the CPD at the GBs occurring at the top surface of the film (indicating downward bending of the CB), while films with (220/204) orientation showed a dip in the CPD at the GBs occurring on the surface of the film (indicating upward bending of the CB).

There have been far fewer studies focused on GBs or sodium in CZTSSe,[24-26] but almost all good CZTSSe devices incorporate sodium since they are fabricated on soda lime glass and processed at high temperature (inherited from CIGSe). Experimentally, two studies have reported that CZTSSe has similar GB physics to CIGSe. Romero et al.[6] compared cathodoluminescence in CZTSe and CIGSe and found a similar red-shift at the GBs in both samples, suggesting similar electrical properties at the GB. Additionally, Clemens et al.[27] showed that a similar positive spike in the CPD appears at the GBs in both CZTSSe and CIGSe. Computationally, *ab initio* calculations have suggested that the GBs of CZTSSe should be significantly less passive[7] than those of CIGSe. If this is true, a downward bend in the CB at the GB (drawing minority carrier electrons into the GB) could lead to increased recombination. As a result, the same nanoscale electrostatics that are beneficial for CIGSe may be deleterious for CZTSSe. More recently, another first principles study suggested that intrinsic CZTSe GBs are not passive due to the formation of Se-Se and Cu-Sn bonds at the GBs that result in deep level states within the bandgap.[28] Further, they suggest a mechanism involving migration of Zn_{Sn}, O_{Se} and Na^{+}_{i} to explain the passivation of these states and the observation of downward band bending in SKPM experiments.

While it is exciting that many of the physical and chemical properties of CZTSSe and CIGSe are similar, CZTSSe devices still lag behind CIGSe devices, and understanding the differences between the materials may reveal opportunities to improve CZTSSe. There are some known differences in the bulk native point defect chemistry. For instance, the formation energies for the acceptor and donor, Cu_{Zn} and Zn_{Cu}, respectively, are small.[29] The result is a highly compensated semiconductor (compared to CIGSe) where these two defects form a neutral defect cluster.

Here, we report experiments that significantly modify the defect chemistry of CZTSSe and enhance its optoelectronic quality and photovoltaic performance. We show the effects of Li doping in CZTSSe by incorporating LiF in the ink used to form the absorber layer. Previously, we reported 8.3% efficient CZTSSe solar cells from a solution of molecular complexes made by dissolving and complexing simple copper, zinc, and tin precursors with thiourea in a DMSO solvent.[30] Compared to other solution phase processing techniques a DMSO molecular ink route has many advantages. It is much safer than hydrazine ink routes,[1, 31] and compared to nanocrystal-ink routes, it has fewer processing steps (simple mixing as compared to NC synthesis and multiple NC washing steps).[32-33] It also provides a unique platform for easily introducing dopants and precisely controlling absorber stoichiometry. Here, we show that active area power conversion efficiencies of 11.8% (with antireflective coating) can be achieved by adding lithium halide salts to a DMSO precursor ink. More importantly, we show that lithium incorporation dramatically changes the nanoscale electrostatics at the grain boundaries by using scanning Kelvin probe microscopy (SKPM). Further, conductive AFM (cAFM) data show that the conductivity in the grain interiors as well as GBs increases by more than an order of magnitude with lithium incorporation. While Li_2ZnSnS_4 is a known wide-bandgap tetrahedrally coordinated semiconductor compound,[34] to our knowledge this is the first report of lithium doping in CZTS, CZTSSe, or CZTSe. This report shows that not only can lithium be used to improve CZTSSe device performance, but that the paradigms inherited from CIGSe do not universally hold for CZTSSe. The knowledge of the defect chemistry and its effects on nanoscale electronic properties learned here provide a pathway for CZTSSe devices to reach much higher efficiencies.

Experimental

Molecular ink preparation and semiconductor film formation. Non-doped and Li-doped inks we prepared as follows: 1140.8 mg $Cu(CH_3COO)_2 \cdot H_2O$ (99.99%, Sigma-Aldrich) and 886.4 mg $SnCl_2 \cdot 2H_2O$ (99.99%, Sigma-Aldrich) were mixed in 5 ml DMSO (99.99%, anhydrous, Sigma-Aldrich) and stirred overnight at room temperature; then 555.0 mg $ZnCl_2$ (99.99%, Sigma-Aldrich) was added and stirred until completely dissolved; finally, 1560.2 mg thiourea (obtained from Sigma-Aldrich and recrystallized from DI water twice; details of recrystallization are given in SI) was added and a transparent, colorless solution was obtained after 2 hours stirring. The solution was split into two equal parts, solution A was diluted by 1.0 ml DMSO (without LiF) and solution B was diluted by 1.0 ml DMSO containing 2 mg LiF (99.99%, anhydrous, Sigma-Aldrich). The atomic ratio in solution B was Li/(Cu+Zn+Sn)=0.011. Both solutions were filtered with 2 μm PTFE filters prior to coating. Inks were spin-coated onto molybdenum coated sodalime glass substrates at a spin speed of 1500 rpm for 60s and then immediately annealed on a hotplate (set point of 540°C) for 2 min. This process was repeated five times to create a layer of approximately 700 nm. All solution preparation, spin-coating, and annealing were conducted in a N_2 filled glovebox system with oxygen and water at less than 10 ppm. The CZTS films were then annealed with elemental Se in

a vented graphite box at temperature of 540°C for 20 min to form CZTSSe.

Solar cell device fabrication and characterization. The selenized film as described above was first submerged in DI water for 5 min and then immediately put into $CdSO_4/NH_4OH$ solution for chemical bath deposition (CBD) of 30 nm CdS as described in previous reports.[30, 35] Then50 nm of i-ZnO and 250 nm ITO are deposited by RF sputtering, and top contacts of Ni/Al are deposited by thermal evaporation of the metals through a shadow mask. Current-voltage (J-V) measurements were performed using a Keithley 2400 source-measure unit in the dark and under 100 mW/cm^2 simulated AM1.5G illumination from a xenon arc lamp with an AM1.5G filter. The incident power was calibrated with a Newport Si reference cell. Each device has an active area of around 0.10 cm^2. However, the exact area for each device was determined using an optical microscope with a distance calibration standard and used for all current density calculations. External quantum efficiency was measured using a chopped monochromatic beam and lock-in amplifier. NIST-traceable calibrated Si and Ge photodiodes were used as references for EQE measurements.

Scanning probe microscopy. Scanning Kevin probe microscopy (SKPM) data were acquired on a MFP-3D-BIO (Asylum Research)-based AFM with custom modifications[36] using 300 kHz Pt-coated cantilevers (BudgetSensor ElectriTap300) for intermittent contact mode techniques. SKPM images were obtained in a two-pass process. Topography was collected in standard AFM intermittent contact mode on the first pass. During the second pass the tip was moved to a constant height above the surface (50 nm) and the surface potential of the same line was measured. During the lift pass an AC bias (700 Hz, 2 V peak-to-peak) was applied to the cantilever from a function generator, combined with a DC bias from the AFM controller via a home-built summing amplifier. The cantilever phase signal from the AFM control was then sent to an SR830 lock-in amplifier, referenced at 700 Hz, and the lock-in signal was returned to the AFM controller to use as a feedback signal. A feedback loop in the controller was set to null this phase signal by adjusting the DC bias applied between the tip and the substrate, thereby measuring the contact potential difference (CPD).[19, 37] Samples for SKPM and conductive atomic force microscopy (cAFM) were prepared as follows: Freshly selenized CZTSSe films were soaked in DI water for 5 minutes, dried with flowing N_2, transferred to a N_2 glove box and assembled in a flow cell. The flow cell was taken out the glove box and imaged under constant nitrogen flow. Details and schematics for the AFM techniques have been reported previously.[36] cAFM maps were also acquired on a MFP-3D-BIO (Asylum Research)-based AFM with custom modifications using gold coated cantilevers (Budget Sensor ContGB-G, spring constant, k = 0.2 N/m) for contact mode techniques. An ORCA (Asylum Research) cantilever holder with sensitivity down to ~1 pA was used to collect changes in current while raster scanning the sample at a scan rate of 0.7 Hz. Images were collected in repulsive mode with a force set point of 96 pN/nm, which simultaneously collected topography and conductivity. Applying a positive bias to the sample allows hole collection while a negative bias on the sample allows electron collection in the cantilever. Samples were variably biased from 0-200 mV.

Results and discussion

Fig. 1a shows the current-voltage (*J-V*) characteristics of the solar cells processed with and without LiF in the precursor ink with a Li/(Cu+Zn+Sn) ratio of 0.011. The maximum active area power conversion efficiencies (PCE) achieved in these devices with and without LiF are 10.5% and 8.7%, respectively (without antireflective coating). The short circuit current density (J_{sc}), open circuit voltage (V_{oc}), and fill factor (*FF*) for the two best devices are 34.9 mA/cm^2, 0.452 V, and 66.4% and 31.9 mA/cm^2, 0.444 V, and 61.3%, respectively. The average solar cell parameters based on 15 devices on the same substrate with standard deviations are summarized in Table 1. Improvements in all device parameters were observed in devices from LiF doped inks. J_{sc} increased by 5.6%, *FF* by 13.4%, and V_{oc} by 5.2%, which lead to a 31% overall efficiency enhancement. The average series resistance (R_s) and shunt resistance (R_{sh}) extracted from the *J-V* curves are 0.38 Ω cm^2 and 4095 Ω for devices with LiF and 0.53 Ω cm^2 and 2781 Ω for devices without LiF. This is a 28% decrease in R_s and a 47% increase in R_{sh}. The lower R_s and higher R_{sh} in devices with LiF compared to that without LiF contribute to the higher *FF*. The average diode quality factor of the non-Li devices is 2.25 and decreases to 1.84 in the doped devices, revealing

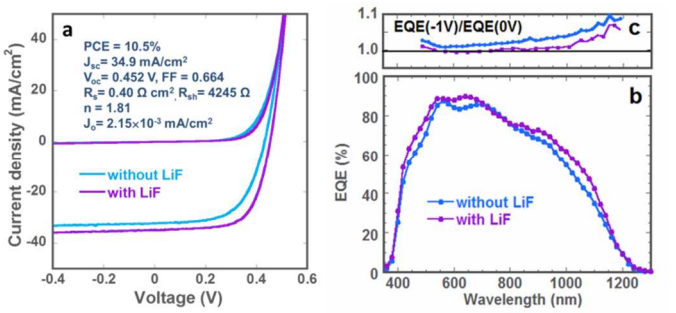

Fig. 1. Current-voltage response and external quantum efficiency of CZTSSe solar cells with and without Li doping. (a) J-V characteristics of the best CZTSSe solar cells measured in dark and under AM 1.5 simulated sunlight with the absorber films processed without and with LiF. The solar cell parameters of the Li-doped champion device are shown in the inset. (b) External quantum efficiency (EQE) of the solar cell. (c) Ratio of EQE measured under -1V bias verse 0V bias.

Physical Chemistry Chemical Physics RSCPublishing

ARTICLE

Table 1. Summary of material and photovoltaic device characteristics of CZTSSe films and devices with and without LiF. The device parameters presented for each sample are average values with standard deviations from 15 solar cells with an active area of 0.10 cm^2 without antireflective coating.

LiF	Cu/ (Zn+Sn)	Zn/Sn	S/(S+Se) XRDa/EDX	Ega (eV)	Jsc (mA/cm2)	Voc (V)	FF (%)	PCE (%)	n	Rs (Ω cm2)	Rsh (Ω)
No	0.74	1.14	0.09/010	1.08±0.023	32.2±0.6	0.426±0.011	57.8±2.6	7.93±0.47	2.25±0.16	0.53±0.11	2781±117
Yes	0.72	1.16	0.10/0.10	1.07±0.007	34.1±0.8	0.448±0.003	65.6±0.9	10.04±0.35	1.84±0.05	0.38±0.02	4095±54

[a] Calculated from fitting the linear portion of $(\ln(1\text{-EQE}))^2$ versus energy.

reduced recombination in the near-junction region of the absorber after Li incorporation. Furthermore, Li doped devices show much higher uniformity as revealed by the much smaller standard deviations in every single device parameter (Table 1). The external quantum efficiency (EQE) spectra and the ratios of reverse biased to non-biased EQE [EQE(-1V)/EQE(0V)] of the solar cells are shown in Fig. 1b and 1c, respectively. EQE above 80% in the visible range with peak plateaus reaching 90% are observed in both films. Given that the reflection losses are expected to be about 10%, the high EQE suggests that the carrier collection efficiency is close to 100% in the CZTSSe near the junction.[38] This is further confirmed by the fact that the quantum efficiency at reverse-bias (Fig. 1c) for visible wavelengths does not change. Devices with Li doping show slightly higher EQE and lower [EQE(-1V)/EQE(0V)] ratio in longer (>800nm) wavelength. The better carrier collection efficiency at near infrared indicates a longer carrier diffusion length. The band gaps extracted from EQE data of lithium doped and non-Li devices are similar, but the band gap variation from Li-doped films is much smaller (Table 1). We note that the improvement in device performance with Li addition is highly reproducible. The average active area efficiency of 90 non-doped devices from 6 separate batches and 150 Li-doped devices from 10 separate batches are 6.7% and 9.5%, respectively. For all side-by-side comparisons of batches of doped and non-doped, the minimum improvement in the doped was greater than 20% in each case.

Fig. 2 shows the scanning electron microscopy (SEM) images of the CZTSSe films processed with and without LiF. From the top view images (Fig. 2a and b), both films show densely packed grains with sizes up to several microns without obvious voids. No significant morphology change is observed with the lithium doped samples. Both cross section images (Fig. 2c and d) show micron size grains extending through the absorber thickness. Some small voids are observed between the absorber layer and the back contact in both films. The X-ray diffraction (XRD) patterns (Fig. S1) show both films are predominantly kesterite phase. However, trace impurities of ZnSe or Cu_2SnSe_3 cannot be ruled out due to the overlap of the main XRD peaks. Both films with randomly oriented texture as determined by Lotgering factors[23] (see Supplementary Information).

The stoichiometry of the absorber material measured by energy dispersive spectroscopy (EDS) is comparable for both films, Cu/(Zn+Sn)=0.74, Zn/Sn=1.14, and S/(S+Se)=0.10 for the film without LiF and Cu/(Zn+Sn)=0.72, Zn/Sn=1.16, and S/(S+Se)=0.10 for the film with LiF. Compared to the metal ratio in the precursor ink [Cu/(Zn+Sn)=0.714, Zn/Sn=1.04], about 10% of the tin is lost during selenization, presumably through the formation of volatile SnS or SnSe.[39] The S/(S+Se) ratios measured by EDS agree well with those calculated from the XRD data (Table 1). No fluoride was detected by EDS, and it is likely lost as part of a volatile compound. EDS is not well suited for the detection of Li due to its small atomic mass. Therefore, the concentrations of Li in the films were determined using inductively coupled plasma mass spectroscopy (ICP-MS). The Li/Cu atomic ratio in the precursor ink is 0.023. After annealing, selenization, and soaking in DI water for 5 min, the Li/Cu atomic ratios were measured to be 7.3×10^{-3}, 3.8×10^{-4}, and 3.9×10^{-5} from samples of films scraped off the substrate (Fig. S2). The decrease of the Li/Cu ratio upon thermal annealing and selenization is very likely due to the evaporation of LiCl[40] and/or Li_2Se[41,42] because of their low melting point and high vapor pressure. The further reduction of Li after DI water soaking is due to dissolution of any Li salts on the film surface. The atomic concentration of lithium in the selenized and washed film is 5.3×10^{16} cm^{-3}.

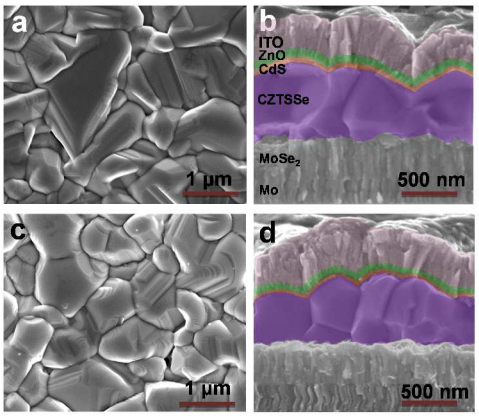

Fig. 2. SEM images of CZTSSe absorber films. (a,b) Top view (a) and cross section (b) SEM images of non-Li films. (c,d) Top view (c) and cross section (d) SEM images of Li-doped CZTSSe films. The cross section images (b) and (d) were measured from cleaved solar cell devices.

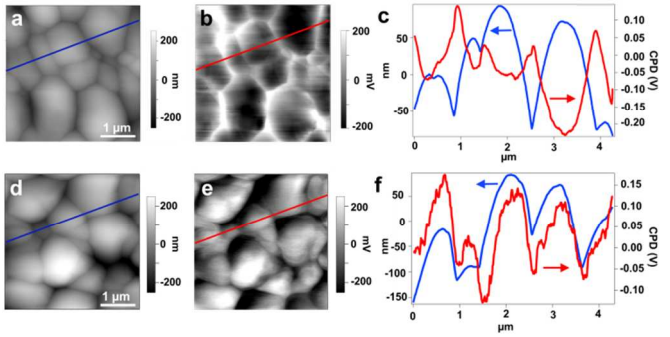

Fig. 3. AFM topography images and SKPM potential maps. (a,b,c) AFM topography (a), SKPM potential map (b), and plots of the topography and potential linescans (c) of CZTSSe films without Li-doping. (d,e,f) AFM topography, (d) potential map (e), and plots of the topography and potential linescans (f) of CZTSSe films with Li-doping.

To confirm the existence of Li on the surface prior to water rinsing and the absence of lithium rich surface compounds after rinsing, we conducted X-ray photoelectron spectroscopy (XPS) measurements (see Supplementary Information, Fig. S3). As expected, Li and Na signals are detected on Li doped films after selenization. Both signals disappear after water soaking In addition, we performed a LiF doping concentration dependence study (Table S1). Device improvements were achieved by doping the ink with LiF amounts as low as Li/(Cu+Zn+Sn)=0.0001. However, increased Li concentrations in the precursor ink resulted in improved device performance and homogeneity of the films for each successive increase.

We have also used SKPM and cAFM to characterize the nanoscale surface potential and conductivity of the CZTSSe absorber layer. Prior to performing these measurements, the films were soaked in DI water to remove any residual salts from the surface. Since no residual Na or Li is detectable on the film surface after DI water soaking (see XPS data in Fig. S3), we infer that the differences measured are the result of changes in the material properties, not an artifact produced by a lithium rich surface layer. Fig. 3 shows both topography and potential maps of CZTSSe films from SKPM and accompanying line scans that show the correlation of topography and potential. In films without lithium doping, we observe a distinct positive peak in the contact potential difference (CPD) at the grain boundaries (Fig. 3a-c), consistent with previous studies of vacuum-deposited CZTSSe films,[27, 43] as well as studies of CIGSe films.[44] This positive spike is consistent with a local accumulation of positive charge at the GB (local increase in the donor concentration), resulting in an electric field and several reports[27, 28, 43] have suggested that this band bending facilitates electron collection through the GBs that is favorable for device performance. However, we show that in higher-performing Li-doped films there is a reversal of the electrostatics at the GBs. We find a dip in the CPD at the GB (Fig. 3d-f) for these Li doped films. This result is consistent with a local accumulation of negative charge at the GB resulting in an electric field and upward band bending towards the GB (Fig. 5b). We conclude that this inversion of electrostatics at the GB is a result of the incorporation of Li in the films and modification of the local defect chemistry. Because the GBs of CZTSSe are less passive than those of CIGSe, the band bending shown in Fig. 5b should be beneficial to device performance by creating a barrier for the minority carrier electrons to cross into the GB.

Assuming a constant bandgap, this upward band bending at the GB is equivalent to a local increase in the acceptor concentration at the GB. However, it is also possible that a thin layer of a lithium compound such as Li_2O, Li_2S, Li_2Se, Li_2SnO_3, or $Li_2ZnSn(S,Se)_4$ forms at the GB, or the lithium acts as a catalyst for the formation of oxide compounds such as SnO_2 or ZnO. Given the large bandgaps of all these compounds, they would result in a type II band offset so long as their work function is not significantly smaller than the bulk CZTSSe. As a result, band diagrams shown in Fig. 5c are also possible. Based on the SKPM data alone, we cannot confirm or rule-out this hypothesis. However, if such layers do form, their effect would be to repel electrons away from the GB and block holes from entering the GB. The dramatic increase in shunt resistance is also likely related to the GBs given the similar morphology of the films with and without lithium. If the GBs were a source of shunts, the creation of upward band bending at the GB would repel minority carrier electrons and increase the shunt resistance.

Li doping also dramatically affects the conductivity as shown in cAFM images (Fig. 4). For these conductivity maps, the current was collected by applying a positive voltage while raster scanning the AFM tip in contact with the sample. Films were

not damaged under repeated scanning (Fig. S4 and S5). The biases applied to films with and without LiF were 100 mV and

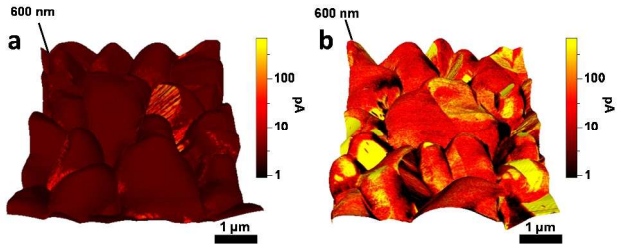

Fig. 4. cAFM images. cAFM conductivity maps overlaid on AFM topography images for films without (a) and with (b) Li doping. Due to the difference in conductivity, the biases applied to film (a) and (b) were 200 mV and 100 mV, respectively.

200 mV, respectively. From Fig. 4a and 4b we observe that the Li-doped film shows greatly improved conductivity, even under a smaller applied bias. The current observed in the doped film is more than one order of magnitude higher than the current observed in the film without doping. Additionally, the conductivity of doped films is improved at both GBs and grain surfaces. We found that the conductivity in films without Li was consistent with that observed in CZTSSe[27] and CIGSe[45] films in the literature, with more conductive GBs than grain surfaces. The higher conductivity of both GBs and grain surfaces in Li-doped films is evidence of lithium being present and active throughout the entire film rather than just at the GBs. From a steric perspective, we note that sodium has a much larger Shannon ionic radius (99 pm for tetrahedral coordination) than copper(I) (60 pm), but lithium (59 pm) is comparable in size to copper(I), zinc (60 pm) and tin(IV) (55 pm). This may allow lithium to be more easily incorporated into the bulk of the CZTSSe lattice and affect the defects and defect clusters in the bulk.

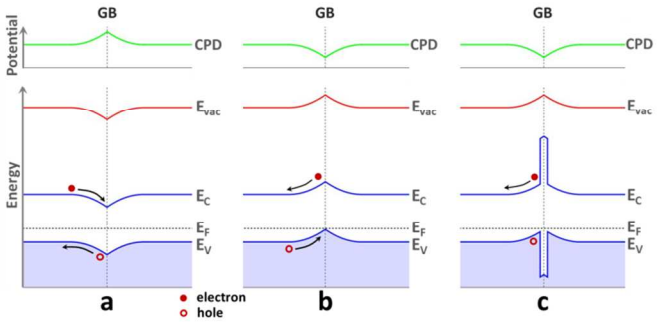

Fig. 5. Schematic of the contact potential difference (CPD) from SKPM and band diagrams across a gain boundary (GB). (a) A positive spike in the CPB at the GB, which is observed for films with no lithium. (b) A dip in the CPD at the GB assuming constant bandgap. (c) A dip in the CPD at the GB along with the formation of a higher bandgap material at the GB. Li-doped films show a dip in the CPD at the GB as shown in panel (b) and (c). However, SKPM cannot distinguish between (b) and (c). The high bandgap material at the GB in part (c) is hypothesized to be Li_2O, Li_2Se, $Li_2ZnSnSe_4$, Li_2SnO_3, SnO_2 or similar compound.

There are several possible mechanisms by which lithium could increase device performance and increase conductivity. Lithium could compete for copper vacancies and thereby: (1) reduce the concentration of the shallow donor Zn_{Cu} (reducing compensation and increasing the p-type carrier concentration), (2) reduce the formation of the neutral defect complexes $[V_{Cu}+Zn_{Cu}]$ and $[Cu_{Zn}+Zn_{Cu}]$, or (3) reduce the formation of the deep acceptor Sn_{Cu}, (reducing SRH recombination and increasing the V_{oc}, carrier diffusion length, and current collection efficiency while decreasing the diode quality factor). Lithium could also (4) form a Se fluxing compound that facilities selenization (reducing the concentration of the donor V_{Se}) or (5) catalyze oxidation at the grain boundaries (forming O_{Se}).[16] It is also possible that (6) Li substitutes on Zn site forming a (likely) shallow acceptor Li_{Zn}. This could reduce the Cu_{Zn} acceptor concentration, but if Li_{Zn} is shallower than Cu_{Zn} then it would lead to a net increase in the p-type carrier concentration due to more complete ionization of the shallower acceptor. Effects (4) and (5) would result in a lower concentration of donor defects and could explain the increase in conductivity. However, because of the predicted high formation energy of V_{Se} (>2.3 eV)[29] we would expect that such defects are primarily present at surfaces and GBs and thus it would not explain the dramatic increase in the conductivity of the crystalline bulk. Similarly, for explanation (3), the predicted formation energy of Sn_{Cu} is large (>1.7 eV) even under Cu-poor conditions.[29] Therefore, the most likely explanations for the increased conductivity and beneficial effect of lithium doping in CZTSSe are: (1) and (2), which are both a result of suppression of Zn_{Cu} donors and (6) which is the replacement of some Cu_{Zn} with shallower Li_{Zn} acceptors.

These conclusions are consistent with the results of Nagaoka et al.[25] who investigated the effects of sodium on CZTS single crystals. They found that sodium increased the effective hole concentration and reduced the thermal activation energy of conduction. This occurred along with a decrease in compensation and an increase in mobility, leading the authors to conclude that sodium occupies copper vacancies and supresses the formation of Zn_{Cu}. Thus we find lithium has many of the same beneficial effects as sodium in the bulk, but the effects on the GBs are very dramatically different. Na doping does not change the electrostatics at the GB.

Direct measurements of carrier concentration would help elucidate exactly which mechanism (or mechanisms) are responsible for the improvements. However, for devices on a conductive back contact, Hall effect measurements are not possible, and thus we use capacitance-voltage (C-V) techniques. While these do not reveal an unambiguous carrier concentration, they do give insight about ionizable defects in the absorber layer of the completed PV devices. Drive-level capacitance profiling (DLCP) is an improvement on conventional C-V profiling. In DLCP the magnitude of the AC signal is extrapolated to zero. As a result, the measured room temperature DLCP concentration (N_{DLCP}) quantifies the

spatially dependent density-of-states that the quasi-Fermi levels sweep through. These include shallow states at the border between the depletion region and quasi-neutral region (that act like dopants) and deeper levels in the depletion region closer to the junction that can respond at the given frequency and temperature (that act as recombination centers). As a result, $N_{DLCP,\ min}$ at room temperature is not simply the carrier concentration, but a combination of shallow and deep defects.

DLCP data were collected for a large number of CZTSSe devices including devices based on DMSO molecular inks with and without LiF. We observe a general trend of increasing V_{oc} with decreasing $N_{DLCP,\ Min}$ (Fig. S6). This is due to passivation of moderately deep defects that improve V_{oc}. However, the average $N_{DLCP,\ min}$ for Li-doped and non-Li devices are $3.5x10^{15}$ cm^{-3} and $5x10^{15}$ cm^{-3}, respectively. The difference is not statistically significant. However, Li containing devices do show statistically significant increases in V_{oc} and decreases in diode quality factor (Table 1), which indicates a reduction of deep defect states (at GB's, in the bulk, or at interfaces) by the addition of lithium. This result suggests that the states being affected are deeper than those that respond to the DLCP measurement at this frequency and temperature. Assuming a thermal emission prefactor similar to that in CIGSe,[46] these states must be deeper than 0.4 eV above the valence band maximum in order not to contribute to N_{DLCP}.

All measurements thus far have point to significant improvements in CZTSSe device performance with increased lithium concentration. Due to the solubility limitations of LiF in DMSO, we also fabricated devices with higher lithium concentrations using LiCl. Using a Li/(Cu+Zn+Sn) ratio of 0.025 in the ink and applying a 150 nm MgF_2 antireflective coating (after Ni/Al evaporation), but all other fabrication steps as described above, we have fabricated the highest efficiency devices. Fig. 6 shows J-V and EQE from the champion device which has a power conversion efficiency of 11.8% under simulated AM1.5 illumination. The crossover of the J-V curves in the champion device indicates a different recombination rate under illumination as compared to dark and will be further investigated in the future.

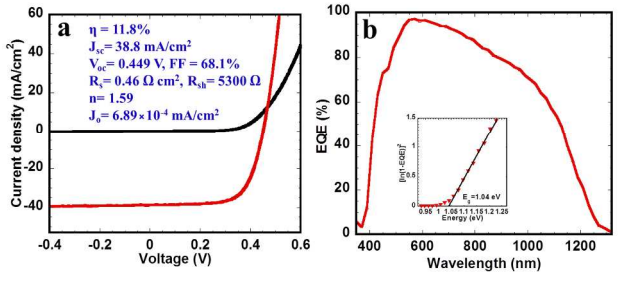

Fig. 6. (a) J-V characteristics of the champion CZTSSe solar cell measured in dark and under AM 1.5 simulated sunlight. (b) External quantum efficiency (EQE) of the solar cell. Inset: Extrapolation of the bandgap from the EQE data.

Conclusions

In summary, we report highly efficient CZTSSe solar cells with lithium halide addition directly from molecular precursor solutions. Structure, morphology, composition, contact potential and conductivity characterizations including XRD, ICPMS, EDS, SEM, XPS, SKPM and cAFM confirm that Li doping greatly improves CZTSSe absorber material electronic quality. Notably, the improvements in device performance achieved with Li doping are accompanied by a concomitant inversion of the potential spike typically observed at CIGSe and CZTSSe grain boundaries. Our observation of a negative spike (a dip) at the grain boundaries challenges the conventional wisdom that a positive spike at the boundaries is an inherent feature of better-performing devices. Additionally, the method of doping demonstrated here (direct addition to a precursor ink) is relatively simple. The 11.8% efficienct device is the highest efficiency CZTSSe solar cell fabricated from solution processing in a non-hydrazine solvent. The additional control over defect chemistry enabled via solution doping opens the door to further improvements in CZTSSe solar cell efficiency, making an important step in the development of scalable manufacturing methods to produce terawatts of high efficiency PV modules.

Acknowledgements

H.W.H. and A.D.C. acknowledge support from the U. S. Department of Energy SunShot Initiative, Next Generation Photovoltaics 2 Program (DE-EE00053210). I.L.B. and H.W.H. acknowledges the National Science Foundation Sustainable Energy Pathways award (CHE-1230615) for supporting the DLCP measurements. D.S.G. and S.M.V. acknowledge the National Science Foundation Sustainable Energy Pathways award (CHE-1230615) for funding the SKPM and cAFM experiments. S.M.V. acknowledges fellowship support from the NDSEG program. A.R.U. acknowledges the financial support from the Swiss National Science Foundation (SNSF) under project number P2EZP2_152168.

Notes and references

[a] Department of Chemical Engineering, University of Washington, Seattle, WA, USA
[b] Department of Chemistry, University of Washington, Seattle, WA, USA
[c] Department of Physics, University of Washington, Seattle, WA, USA
[d] Molecular Engineering & Sciences Institute, University of Washington, Seattle, WA, USA
*Email: h2@uw.edu

Electronic Supplementary Information (ESI) available: X-ray diffraction (XRD), scanning electron microscopy (SEM), inductively coupled plasma mass spectroscopy (ICPMS), drive-level capacitance profiling (DLCP), X-ray photoelectron spectroscopy (XPS), recrystallizaiton of thiourea, and Li doping concentration study.

1. W. Wang, M. T. Winkler, O. Gunawan, T. Gokmen, T. K. Todorov, Y. Zhu and D. B. Mitzi, *Adv. Energy Mater.*, 2013, **4**, 1301465.

2. A. Chirila, P. Reinhard, F. Pianezzi, P. Bloesch, A. R. Uhl, C. Fella, L. Kranz, D. Keller, C. Gretener, H. Hagendorfer, D. Jaeger, R. Erni, S. Nishiwaki, S. Buecheler and A. N. Tiwari, *Nat. Mater.,* 2013, **12**, 1107-1111.
3. P. Jackson, D. Hariskos, E. Lotter, S. Paetel, R. Wuerz, R. Menner, W. Wischmann and M. Powalla, *Prog. Photovoltaic,* 2011, **19**, 894-987. 4.
4. U. Rau and J. H. Werner, *Appl. Phys. Lett.*, 2004, **84**, 3735-3737.
5. A. Walsh, S. Chen, S.-H. Wei and X.-G. Gong, *Adv. Energy Mater.*, 2012, **2**, 400-409.
6. M. J. Romero, H. Du, G. Teeter, Y. F. Yan and M. M. Al-Jassim, *Phys. Rev. B*, 2011, **84**, 5.
7. J. Li, D. B. Mitzi and V. B. Shenoy, *Acs Nano*, 2011, **5**, 8613-8619.
8. T. Gokmen, O. Gunawan, T. K. Todorov and D. B. Mitzi, *Appl. Phys. Lett.*, 2013, **103**, 103506.
9. J. Hedstrom, H. Ohlsen, M. Bodegard, A. Kylner, L. Stolt, D. Hariskos, M. Ruckh and H. Schock, *Proceedings of the 23th IEEE PVSC,* 1993, 364-371.
10. B. M. Basol, V. K. Kapur, C. R. Leidholm, A. Minnick, A. Halani and Ieee, *Proceedings of the 24th IEEE PVSC,* 1994, 148-151.
11. D. Cahen and R. Noufi, *Appl. Phys. Lett.*, 1989, **54**, 558-560.
12. M. A. Contreras, B. Egaas, P. Dippo, J. Webb, J. Granata, K. Ramanathan, S. Asher, A. Swartzlander, R. Noufi and Ieee, *Proceedings of the 26th IEEE PVSC,* 1997, 359-362.
13. D. W. Niles, K. Ramanathan, F. Hasoon, R. Noufi, B. J. Tielsch and J. E. Fulghum, *J. Vac. Sci. Technol. A*, 1997, **15**, 3044-3049.
14. T. Nakada, D. Iga, H. Ohbo and A. Kunioka, *Jpn. J. Appl. Phys. Part 1,* 1997, **36**, 732-737.15.
15. L. Kronik, D. Cahen and H. W. Schock, *Adv. Mater.*, 1998, **10**, 31.
16. L. Kronik, U. Rau, J.-F. Guillemoles, D. Braunger, H.-W. Schock and D. Cahen, *Thin Solid Films*, 2000, **361–362**, 353-359.
17. M. Igalson, A. Kubiaczyk, P. Zabierowski, M. Bodegard and K. Granath, *Thin Solid Films*, 2001, **387**, 225-227.
18. S. H. Wei, S. B. Zhang and A. Zunger, *J. Appl. Phys.*,1999, **85**, 7214-7218.
19. C. S. Jiang, R. Noufi, K. Ramanathan, J. A. AbuShama, H. R. Moutinho and M. M. Al-Jassim, *Appl. Phys. Lett.*, 2004, **85**, 2625-2627.
20. P. T. Erslev, J. W. Lee, W. N. Shafarman and J. D. Cohen, *Thin Solid Films*, 2009, **517**, 2277-2281.
21. D. Braunger, D. Hariskos, G. Bilger, U. Rau and H. W. Schock, *Thin Solid Films*, 2000, **361**, 161-166.
22. Y. Yan, C. S. Jiang, R. Noufi, S.-H. Wei, H. R. Moutinho and M. M. Al-Jassim, *Phys. Rev. Lett.*, 2007, **99**.
23. G. Hanna, T. Glatzel, S. Sadewasser, N. Ott, H. P. Strunk, U. Rau and J. H. Werner, *Appl. Phys. A,* 2006, **82**, 1-7.
24. R. Haight, X. Shao, W. Wang and D. B. Mitzi, *Appl. Phys. Lett.*, 2014, **104**.
25. A. Nagaoka, H. Miyake, T. Taniyama, K. Kakimoto, Y. Nose, M. A. Scarpulla and K. Yoshino, *Appl. Phys. Lett.*, 2014, **104**.
26. T. Gershon, B. Shin, N. Bojarczuk, M. Hopstaken, D. B. Mitzi and S. Guha, *Adv. Energy Mater.*, 2015, **5**.
27. J. B. Li, V. Chawla and B. M. Clemens, *Adv. Mater.*, 2012, **24**, 720.
28. W.-J. Yin, Y. Wu, S.-H. Wei, R. Noufi, M. M. Al-Jassim and Y. Yan, *Advanced Energy Materials*, 2014, **4**, n/a-n/a.
29. S. Chen, A. Walsh, X.-G. Gong and S.-H. Wei, *Adv. Mater.*, 2013, **25**, 1522-1539.
30. H. Xin, J. K. Katahara, I. L. Braly and H. W. Hillhouse, *Adv. Energy Mater.*, 2014, **4**.
31. T. K. Todorov, J. Tang, S. Bag, O. Gunawan, T. Gokmen, Y. Zhu and D. B. Mitzi, *Adv. Energy Mater.*, 2013, **Vol. 3**, 34-38.
32. Q. Guo, G. M. Ford, W. C. Yang, B. C. Walker, E. A. Stach, H. W. Hillhouse and R. Agrawal, *J. Amer. Chem. Soc.*, 2010, **132**, 17384-17386.
33. K. E. Roelofs, Q. J. Guo, S. Subramoney and J. V. Caspar, *J. Mater. Chem. A*, 2014, **2**, 13464-13470.
34. J. W. Lekse, B. M. Leverett, C. H. Lake and J. A. Aitken, *J. Solid State Chem.*, 2008, **181**, 3217-3222.
35. W. Ki and H. W. Hillhouse, *Adv. Energy Mater.*, 2011, **1**, 732-735.
36. L. S. C. Pingree, O. G. Reid and D. S. Ginger, *Adv. Mater.*, 2009, **21**, 19-28.
37. C. Groves, O. G. Reid and D. S. Ginger, *Acc. Chem. Res.*, 2010, **43**, 612-620.
38. S. S. Hegedus and W. N. Shafarman, *Prog. Photovoltaics*, 2004, **12**, 155-176.
39. J. J. Scragg, J. T. Wätjen, M. Edoff, T. Ericson, T. Kubart and C. Platzer-Björkman, *J. Amer. Chem. Soc.*, 2012.
40. http://chemister.ru/Database/properties-en.php?dbid=1&id=614.
41. P. T. Cunningh, S. A. Johnson and E. J. Cairns, *J. Electrochem. Soc.*, 1971, **118**, 1941-1944.
42. http://chemspider.com/Chemical-Structure.74834.html.
43. G. Y. Kim, J. R. Kim, W. Jo, D. H. Son, D. H. Kim and J. K. Kang, *Nanoscale Res. Lett.*, 2014, **9**.
44. C. S. Jiang, R. Noufi, J. A. AbuShama, K. Ramanathan, H. R. Moutinho, J. Pankow and M. M. Al-Jassim, *Appl. Phys. Lett.*, 2004, **84**, 3477-3479.
45. S. Sadewasser, D. Abou-Ras, D. Azulay, R. Baier, I. Balberg, D. Cahen, S. Cohen, K. Gartsman, K. Ganesan, J. Kavalakkatt, W. Li, O. Millo, T. Rissom, Y. Rosenwaks, H. W. Schock, A. Schwarzman and T. Unold, *Thin Solid Films*, 2011, **519**, 7341-7346.
46. J. T. Heath, J. D. Cohen and W. N. Shafarman, *J. Appl. Phys.*, 2004, **95**, 1000-1010.

